ARL-TR-10127 ● JULY 2025

# Influence of an External Magnetic Field on the Reactions of Magnet-in-Ferroelectric Energetic Crystals

by Jennifer L. Gottfried and Shenqiang Ren

## NOTICES

### Disclaimers

The findings in this report are not to be construed as an official Department of the Army position unless so designated by other authorized documents.

Citation of manufacturer's or trade names does not constitute an official endorsement or approval of the use thereof.

Destroy this report when it is no longer needed. Do not return it to the originator.

ARL-TR-10127 ● JULY 2025


# Influence of an External Magnetic Field on the Reactions of Magnet-in-Ferroelectric Energetic Crystals

**Jennifer L. Gottfried**
*DEVCOM Army Research Laboratory*

**Shenqiang Ren**
*University of Maryland*

# REPORT DOCUMENTATION PAGE

| 1. REPORT DATE | 2. REPORT TYPE | 3. DATES COVERED | |
|---|---|---|---|
| | | START DATE | END DATE |
| July 2025 | Technical Report | 25 March 2025 | 11 June 2025 |

**4. TITLE AND SUBTITLE**
Influence of an External Magnetic Field on the Reactions of Magnet-in-Ferroelectric Energetic Crystals

| 5a. CONTRACT NUMBER | 5b. GRANT NUMBER | 5c. PROGRAM ELEMENT NUMBER |
|---|---|---|
| 5d. PROJECT NUMBER | 5e. TASK NUMBER | 5f. WORK UNIT NUMBER |

**6. AUTHOR(S)**
Jennifer L. Gottfried and Shenqiang Ren

**7. PERFORMING ORGANIZATION NAME(S) AND ADDRESS(ES)**
DEVCOM Army Research Laboratory
ATTN: FCDD-RLA-WA
Aberdeen Proving Ground, MD 21005

**8. PERFORMING ORGANIZATION REPORT NUMBER**
ARL-TR-10127

| 9. SPONSORING/MONITORING AGENCY NAME(S) AND ADDRESS(ES) | 10. SPONSOR/MONITOR'S ACRONYM(S) | 11. SPONSOR/MONITOR'S REPORT NUMBER(S) |
|---|---|---|
| | | |

**12. DISTRIBUTION/AVAILABILITY STATEMENT**
DISTRIBUTION STATEMENT A. Approved for public release: distribution unlimited.

**13. SUPPLEMENTARY NOTES**
ORCIDs: Jennifer Gottfried, 0000-0002-1282-1928; Shenqiang Ren, 0000-0002-9987-3316

**14. ABSTRACT**
The magnetic properties of the molecular energetic ferroelectric material imidazolium perchlorate ($ImClO_4$) were manipulated by adding layers of magnets to the $ImClO_4$ crystals to create 2-D materials containing chromium and either lithium or vanadium. The influence of an external magnetic field generated by stacked permanent magnets (up to 0.78 T) on the energy release of these materials following rapid heating was investigated using the magnetic-field-enhanced laser-induced air shock from energetic materials (B-LASEM) technique. The energy release in three distinct time regimes—during the laser-induced plasma (<13 μs), post-plasma combustion reactions (tens to hundreds of microseconds), and self-sustained combustion reactions on the millisecond timescale—were compared with and without the magnetic field. Estimated detonation velocities and detonation temperatures were calculated and compared with predicted values. Our results demonstrate that magnetic coupling can be used to influence when and how much energy is released by energetic materials under detonation-like conditions using a high-throughput, microscale experiment.

**15. SUBJECT TERMS**
energetic material, molecular ferroelectric, magnetic field coupling, laser-induced air shock from energetic materials, LASEM, Weapons Sciences

| 16. SECURITY CLASSIFICATION OF: | | | 17. LIMITATION OF ABSTRACT | 18. NUMBER OF PAGES |
|---|---|---|---|---|
| a. REPORT | b. ABSTRACT | C. THIS PAGE | | |
| UNCLASSIFIED | UNCLASSIFIED | UNCLASSIFIED | UU | 36 |

| 19a. NAME OF RESPONSIBLE PERSON | 19b. PHONE NUMBER *(Include area code)* |
|---|---|
| Jennifer L. Gottfried | (520) 691-6002 |

**STANDARD FORM 298 (REV. 5/2020)**
*Prescribed by ANSI Std. Z39.18*

## Contents

## List of Figures

## List of Tables

## Acknowledgments

This work was funded by ARL's 6.2 project "Explosives for Long Range Collaborative Engagements" under the Long Range Distributed and Collaborative Engagements Essential Research Program in support of the Army's top modernization priority Long Range Precision Fires. The synthesis and development of the magnet-in-ferroelectric crystals was funded by the Army Research Office under award W911NF-25-2-0038 (University of Maryland, College Park; principal investigator: Shenqiang Ren).

# 1. Introduction

Imidazolium perchlorate ($ImClO_4$) is a molecular ferroelectric salt that has previously been investigated in our laboratory for its microsecond-timescale energetic properties.[1–4] Although it has a relatively unfavorable oxygen balance (–38%) and an underwhelming estimated detonation velocity of 7.20 ±0.27 km/s—comparable to the explosive hexanitrostilbene (HNS), assuming $ImClO_4$ is detonable and can be pressed to the theoretical maximum density (TMD)—it was speculated that its unique ferroelectric properties could make it suitable for specialized energetic applications. Ferroelectric materials have a permanent electric dipole that can be reversibly changed through the application of an external voltage, mechanical impact (piezoelectric), or temperature change (pyroelectric). In contrast to the more commonly studied perovskite oxides, organic ferroelectric materials are flexible, lightweight, and easier to process—typically at the expense of smaller polarization and piezoelectric coefficients.[5] Although depolarizing the $ImClO_4$ did not influence the microsecond-timescale energy release, depolarization of another energetic molecular ferroelectric salt $[Hdabco]ClO_4$ (DABCO = 1,4diazabicyclo[2.2.2]octane) reduced the estimated detonation velocity measured using the laser-induced air shock from energetic materials (LASEM) technique[6] from 7.79 ±0.25 km/s to 6.69 ±0.21 km/s.[7]

Recently, a new class of materials referred to as magnet-in-ferroelectric crystals was developed to enable investigation of the ferroelectric and magnetic coupling effects.[8] The 2-D magnetic materials $Li_{0.7}Cr(pyz)_2Cl_{0.7}$ (LCPC, pyz=pyrazine)[8,9] and $V[Cr(CN)_6]_{0.85} \cdot 4.2\ H_2O$ (V-Cr PBA, Prussian blue analog)[10] were selected as the potential magnetic components in combination with $ImClO_4$ as the ferroelectric crystal. While LCPC is considered a hard magnet with strong ferromagnetism, PBA is a soft magnet that is weakly ferromagnetic. Here, we used a recently developed variant of the LASEM technique that incorporates an external magnetic field to influence the energy release (B-LASEM[11,12]) to evaluate $ImClO_4$ as well as the LCPC-$ImClO_4$ and VBA-$ImClO_4$ composites.

# 2. Experimental

## 2.1 Samples

The $ImClO_4$ samples were provided to the U.S. Army Combat Capabilities Development Command Army Research Laboratory for LASEM analysis. The PBA-$ImClO_4$ (black and white material) and LCPC-$ImClO_4$ (red material) composites were received in January 2024 (and analyzed in March 2025), while the

$ImClO_4$ (clear crystal) analyzed in this work was left over from a previous study several years prior; all samples were stored in a dry box prior to analysis. The composites were prepared in a 1:1 molar ratio. The samples were prepared for LASEM analysis by crushing and spreading approximately 20 mg of material on double-sided tape affixed to a glass microscope slide.

## 2.2 B-LASEM

The B-LASEM system used in this work[12] (Figure 1) is a modification of the LASEM-420 system previously described in detail[4] and a previous version of B-LASEM that incorporated a weak electromagnet.[11] To investigate the influence of a magnetic field on the energy release of laser-excited materials in three distinct time regimes (<10 µs, tens to hundreds of microseconds, and 1–100 ms), the sample was placed on a permanent magnet setup consisting of two neodymium permanent magnets (50.8 mm [2 inch] diameter, 12.7 mm [0.5 inch] thick, N52 grade) stacked and rotated such that the sample was placed on the edge of the magnet at the precise locations with the strongest magnetic field (+0.78 T or –0.73 T at either pole). The magnetic flux lines exit the north pole (positive magnetic-flux density *B*, denoted "P" in the sample labels) and enter the south pole (negative *B*, denoted "N" in the sample labels); thus, the electrons flow in opposite directions parallel to the sample surface depending on which pole the sample is above. The decrease in *B* in the air above the sample surface (where the laser-initiated chemical reactions occur) is shown in Figure 2.

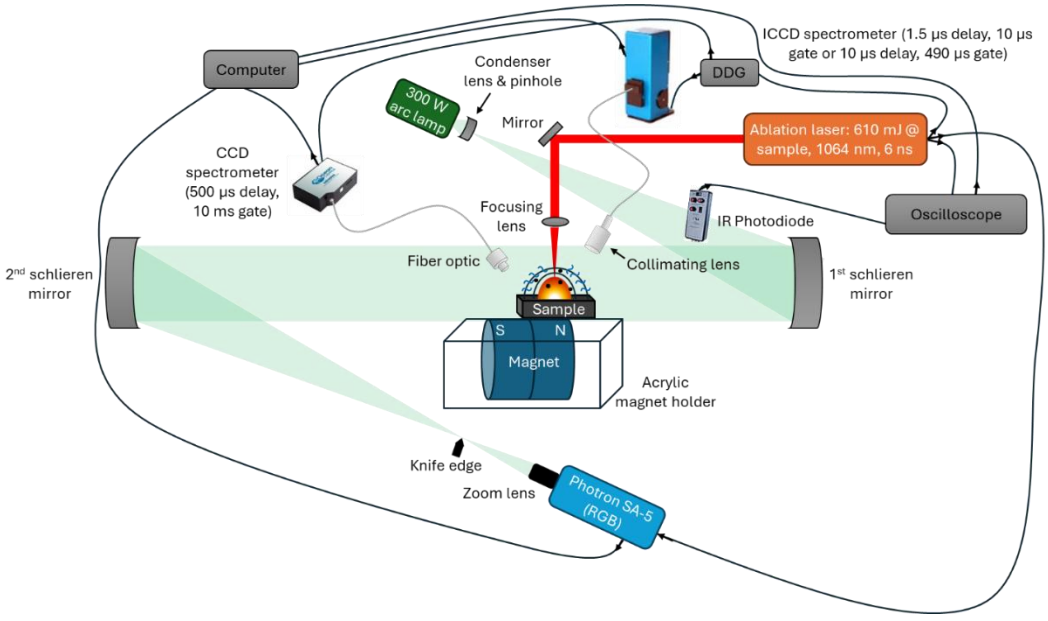


**Figure 1. Experimental schematic for the B-LASEM system as configured for the current study; figure is not to scale.**

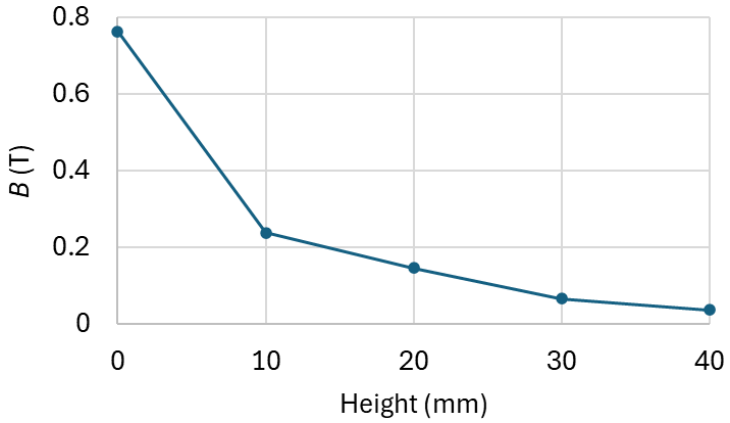


**Figure 2. Magnetic-flux density *B* as a function of the height above the surface of the magnet edge.**

A high-energy nanosecond-pulsed laser is focused just below the sample surface to ablate, ionize, and excite the material into a laser-induced plasma that emits radiation at wavelengths characteristic of the species reacting in the plasma. A laser-induced shock wave expands into the air above the sample surface, and particles are ejected off the sample surface to react during post-plasma combustion reactions. High-speed schlieren imaging with a color camera (red–green–blue [RGB]) is used to record the expansion of the shock wave, plasma plume, and subsequent combustion reactions; the 4.25-inch-diameter schlieren mirrors have a 45-inch focal length and are separated by 90 inches. High-speed schlieren videos (20 replicates each) were obtained at 420 kfps with an image size of 832 × 16 pixels and an exposure time of 369 ns to track the expansion of the laser-induced shock wave into the air above the samples up to 112 µs. Custom MATLAB code was used to measure the time-resolved shock wave positions[13,14]; for these measurements, the shock position was rounded down to the nearest pixel.[15] The code also automatically fits the data to determine the extent of energy release on the microsecond timescale using parameters such as the characteristic laser-induced shock velocity, the Dewey shock velocity, and the speed of sound in air for the acoustic wave.[16] For the current samples, no significant differences in calculated parameters were observed when the shock position was rounded up to the next pixel. Additional custom code was used to perform multiple comparison of means tests on the resulting calculated parameters to determine the statistical significance of the differences in the average parameters for each sample.[17]

Two spectrometers monitored the spatially and temporally integrated plasma or combustion emission. A digital delay generator (DDG) controlled the gate delays and gate widths for the spectrometers; the Q-switch out trigger from the laser initiated all data collection. A high-resolution echelle spectrometer with an intensified charge-coupled device (ICCD) detector resolved the spatially and

temporally integrated emission from the post-plasma combustion (gate delay = 10 μs, gate width = 490 μs) or laser-induced plasma (gate delay set to 1.5 μs to avoid the continuum emission, gate width set to 10 μs over the plasma lifetime). The post-plasma combustion emission from the first 10 laser shots was saved; the second set of 10 laser shots was used to record the laser-induced plasma emission. A charge-coupled device (CCD) spectrometer was set to record the combustion emission spectra from 500 μs to 10.5 ms to focus on the self-sustained combustion reactions. An IR-sensitive photodiode (900–1700 nm) was used to monitor the time-resolved emission from self-sustained combustion on the millisecond timescale; the reported signals from the photodiode were corrected for the instrument gain ($1 \times 10^3$) and converted to optical power. The first five laser shots were widely spaced along the sample surface to ensure sufficient ejected particles for the self-sustained combustion reactions; the IR traces and CCD spectra for these first five shots were saved for each sample. Subsequent laser shots (for which only the shock data and ICCD spectra were saved) were more closely spaced since that data does not significantly depend on the amount of intact particles ejected from the surface by the shock wave. All error bars in the figures represent 95% confidence intervals.

## 3. Results

### 3.1 High-Speed Schlieren Imaging of Laser-Induced Shock Waves

Representative snapshots from the high-speed schlieren videos for each sample with and without the magnetic field are shown in Figure 3. The sample is located on the far left of the image, while the laser propagates from right to left; the Q-switch from the laser triggers the camera. Each frame in the vertically oriented image montage is separated by 2.38 μs (up to nearly 148 μs). The neat $ImClO_4$ has very little plasma emission (1st frame), which is slightly enhanced by the presence of an external magnetic field (Figure 3a–c). The plume of hot gaseous products grows to approximately the same height with or without the magnetic field. Unlike the $ImClO_4$, the PBA-$ImClO_4$ shows substantial combustion emission in the first few tens of microseconds (Figure 3d). This combustion emission lasts longer under the external magnetic field (Figure 3e–f). LCPC-$ImClO_4$ also has longer-lasting emission than the neat $ImClO_4$ (Figure 3g–i).

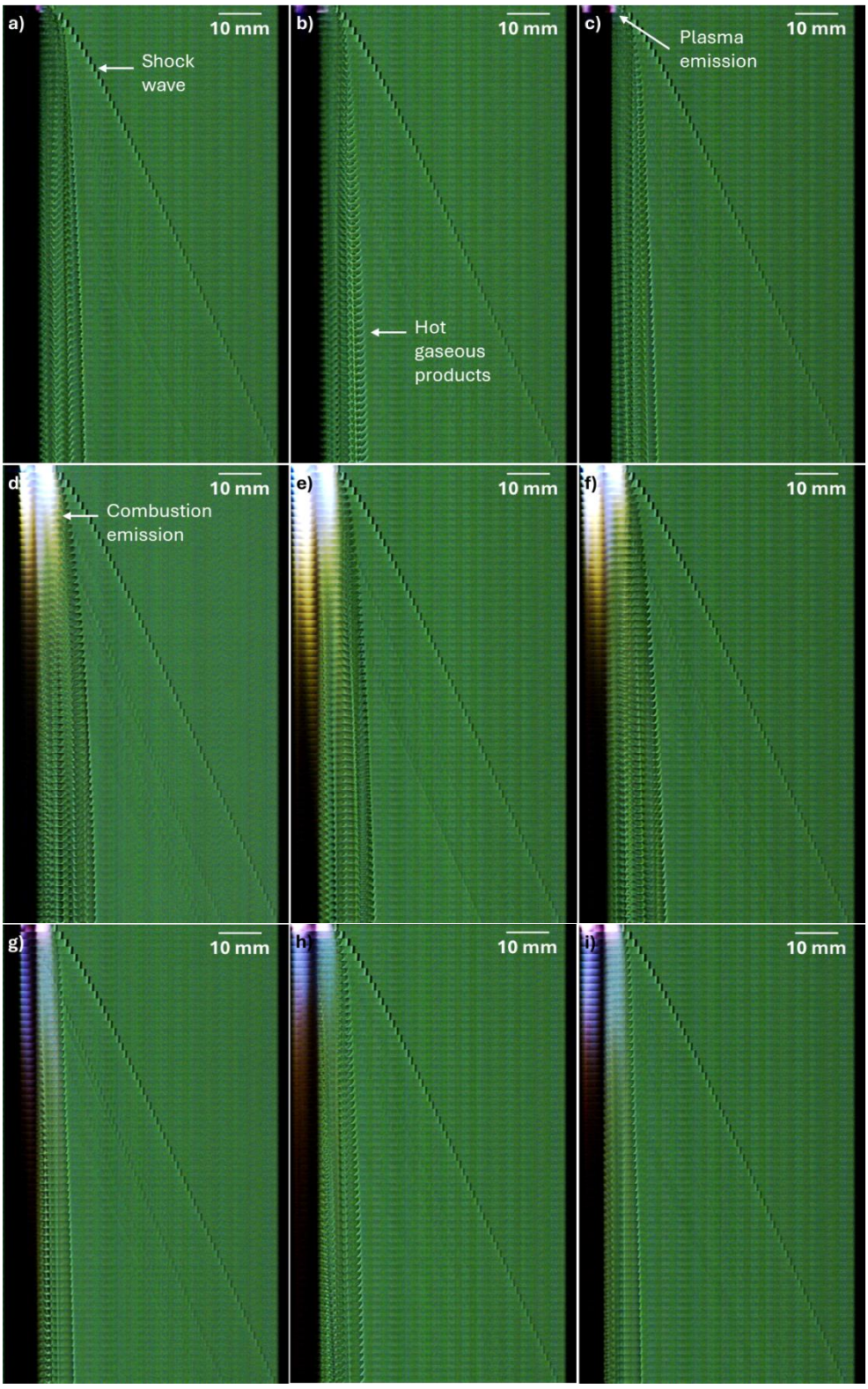


**Figure 3. Snapshots from the high-speed schlieren imaging of the a) $ImClO_4$, b) $ImClO_4$ (+0.78 T), c) $ImClO_4$ (–0.73 T), d) PBA-$ImClO_4$, e) PBA-$ImClO_4$ (+0.78 T), f) PBA-$ImClO_4$ (–0.73 T), g) LCPC-$ImClO_4$, h) LCPC-$ImClO_4$ (+0.78 T), and i) LCPC-$ImClO_4$ (–0.73 T). The images have been rotated 90° and cropped identically, with the brightness increased 80%.**

Figure 4 compares the characteristic laser-induced shock velocities determined by the y-intercept of a 5th order polynomial to the shock velocity versus time to the Dewey shock velocity determined by the value of the Dewey equation fit to the same data at 13 μs.[6] The former (y-axis) quantifies the early microsecond timescale energy release since it is an extrapolation to time zero, while the latter (x-axis) quantifies the energy released in the laser-induced plasma over the entire plasma lifetime. For most conventional military explosives, the two parameters are strongly linearly correlated—i.e., higher characteristic laser-induced shock velocities correspond to proportionally higher Dewey shock velocities. Deviations from this linear behavior help differentiate energetic materials that react earlier in the plasma from those that react later. For example, energetic formulations with slower reacting ingredients like aluminum tend to have much higher contributions to the Dewey shock velocity. The linear fit trendline in Figure 4 is provided as a guideline to the eye. Adding an external magnetic field lowers the characteristic laser-induced shock velocity for the neat $ImClO_4$ and for the PBA-$ImClO_4$—but does not significantly affect the Dewey shock velocity. In contrast, the characteristic laser-induced shock velocities increase for LCPC-$ImClO_4$ in the presence of the magnetic field—as do the Dewey shock velocities. This behavior is evidently a result of the differences in magnetic coupling with the stronger magnet in LCPC-$ImClO_4$ compared with having no magnet ($ImClO_4$) or a weaker magnet (PBA-$ImClO_4$).

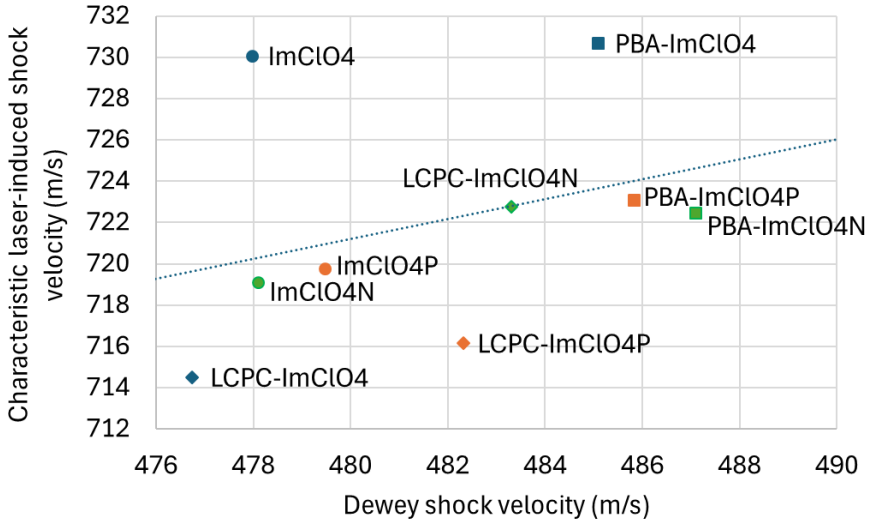


**Figure 4. Comparison of the characteristic laser-induced shock velocities and Dewey shock velocities for the $ImClO_4$ (circles), PBA-$ImClO_4$ (squares), and LCPC-$ImClO_4$ (diamonds) with (orange = +0.78 T, green = –0.73 T) and without (blue) an external magnetic field.**

Differences in the speeds of sound in air determined from a double exponential fit[6] were observed between the samples with or without the magnetic field (Figure 5). The speed of sound in air is a function of the temperature, pressure, and humidity of the air—with temperature having the largest effect. As shown in Figure 3, the

surrounding air is heated by the laser-induced plasma and subsequent exothermic reactions. This results in faster speeds of sound for more energetic materials. The presence of the external magnetic field increases the speeds of sound in air for all materials—with the largest effects seen for the magnet-in-ferroelectric crystals.

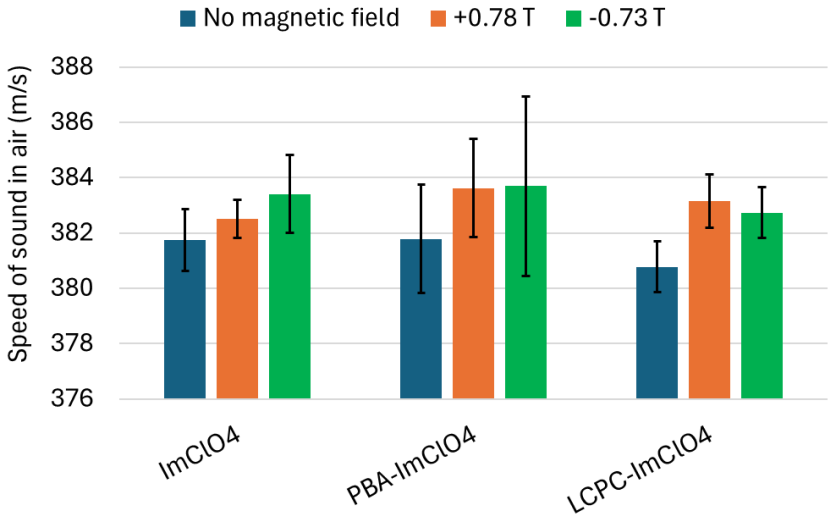


**Figure 5. Comparison of the fitted speeds of sound for the laser-induced shock wave (>100 μs) from the $ImClO_4$, PBA-$ImClO_4$, and LCPC-$ImClO_4$ with (orange = +0.78 T, green = –0.73 T) and without (blue) an external magnetic field.**

Multiple comparison of means testing was performed to assess the statistical significance of the observed differences in characteristic laser-induced shock velocities (Table 1), Dewey shock velocities (Table 2), and speeds of sound in air (Table 3). The characteristic laser-induced shock velocities for LCPC-$ImClO_4$ are significantly lower than those of $ImClO_4$ and PBA-$ImClO_4$ at the 95% confidence level (Table 1). The $ImClO_4$ shows the most significant drop in characteristic laser-induced shock velocities in the presence of the magnetic field. Much more significant changes in the Dewey shock velocities were observed for all samples (Table 2). The neat PBA-$ImClO_4$ has a significantly higher Dewey shock velocity than the neat $ImClO_4$, presumably due to increased combustion reactions (Figure 3d). Although the magnetic field did not significantly change the Dewey shock velocities for $ImClO_4$ or PBA-$ImClO_4$, they were significantly higher for LCPC- $ImClO_4$ in the presence of the magnetic field. The speed of sound in air for PBA-$ImClO_4$ significantly increased in the presence of the magnetic field, indicating additional combustion reactions further heated the surrounding air (Table 3). Although the speed of sound in air for LCPC-$ImClO_4$ also increased in the presence of the magnetic field, those increases were slightly less significant (~86%–93% confidence level); the increases in speeds of sound in air for $ImClO_4$ under the influence of the magnetic field were significant at the 70%–86%

confidence level. Figure 5 shows the speeds of sound in air determined from the fit to the averaged shock velocity data, while the multiple comparison of means testing (Table 3) uses the values from the individual fits, which can have different means compared with the fit of the averaged data, to determine the statistical significance in the means.

**Table 1. Multiple comparison of means test results for the characteristic laser-induced shock velocities; p-values <0.05 are shaded in dark red and indicate the average values are different at the 95% confidence level, while p-values shaded in green show no statistical difference.**

| | $ImClO_4$ | $ImClO_4P$ | $ImClO_4N$ | PBA-$ImClO_4$ | PBA-$ImClO_4P$ | PBA-$ImClO_4N$ | LCPC-$ImClO_4$ | LCPC-$ImClO_4P$ | LCPC-$ImClO_4N$ |
|---|---|---|---|---|---|---|---|---|---|
| $ImClO_4$ | | 1.17E-01 | 9.54E-02 | 9.26E-01 | 2.87E-01 | 2.46E-01 | 2.00E-02 | 3.49E-02 | 2.64E-01 |
| $ImClO_4P$ | 1.17E-01 | | 9.20E-01 | 9.70E-02 | 6.12E-01 | 6.80E-01 | 4.30E-01 | 5.82E-01 | 6.49E-01 |
| $ImClO_4N$ | 9.54E-02 | 9.20E-01 | | 7.86E-02 | 5.43E-01 | 6.08E-01 | 4.90E-01 | 6.53E-01 | 5.78E-01 |
| PBA-$ImClO_4$ | 9.26E-01 | 9.70E-02 | 7.86E-02 | | 2.48E-01 | 2.11E-01 | 1.58E-02 | 2.78E-02 | 2.27E-01 |
| PBA-$ImClO_4P$ | 2.87E-01 | 6.12E-01 | 5.43E-01 | 2.48E-01 | | 9.24E-01 | 1.97E-01 | 2.91E-01 | 9.58E-01 |
| PBA-$ImClO_4N$ | 2.46E-01 | 6.80E-01 | 6.08E-01 | 2.11E-01 | 9.24E-01 | | 2.32E-01 | 3.37E-01 | 9.65E-01 |
| LCPC-$ImClO_4$ | 2.00E-02 | 4.30E-01 | 4.90E-01 | 1.58E-02 | 1.97E-01 | 2.32E-01 | | 8.04E-01 | 2.16E-01 |
| LCPC-$ImClO_4P$ | 3.49E-02 | 5.82E-01 | 6.53E-01 | 2.78E-02 | 2.91E-01 | 3.37E-01 | 8.04E-01 | | 3.15E-01 |
| LCPC-$ImClO_4N$ | 2.64E-01 | 6.49E-01 | 5.78E-01 | 2.27E-01 | 9.58E-01 | 9.65E-01 | 2.16E-01 | 3.15E-01 | |

**Table 2. Multiple comparison of means test results for the Dewey shock velocities; p-values <0.05 are shaded in dark red and indicate the average values are different at the 95% confidence level, while p-values shaded in green show no statistical difference.**

| | $ImClO_4$ | $ImClO_4P$ | $ImClO_4N$ | PBA-$ImClO_4$ | PBA-$ImClO_4P$ | PBA-$ImClO_4N$ | LCPC-$ImClO_4$ | LCPC-$ImClO_4P$ | LCPC-$ImClO_4N$ |
|---|---|---|---|---|---|---|---|---|---|
| $ImClO_4$ | | 6.02E-01 | 2.88E-01 | 2.06E-06 | 9.42E-07 | 2.55E-06 | 4.17E-01 | 1.66E-01 | 2.45E-02 |
| $ImClO_4P$ | 6.02E-01 | | 5.87E-01 | 1.96E-05 | 9.47E-06 | 2.38E-05 | 1.86E-01 | 3.86E-01 | 8.25E-02 |
| $ImClO_4N$ | 2.88E-01 | 5.87E-01 | | 1.67E-04 | 8.63E-05 | 2.00E-04 | 6.38E-02 | 7.45E-01 | 2.31E-01 |
| PBA-$ImClO_4$ | 2.06E-06 | 1.96E-05 | 1.67E-04 | | 8.63E-01 | 9.62E-01 | 6.13E-08 | 5.46E-04 | 8.88E-03 |
| PBA-$ImClO_4P$ | 9.42E-07 | 9.47E-06 | 8.63E-05 | 8.63E-01 | | 8.25E-01 | 2.63E-08 | 2.93E-04 | 5.37E-03 |
| PBA-$ImClO_4N$ | 2.55E-06 | 2.38E-05 | 2.00E-04 | 9.62E-01 | 8.25E-01 | | 7.72E-08 | 6.45E-04 | 1.02E-02 |
| LCPC-$ImClO_4$ | 4.17E-01 | 1.86E-01 | 6.38E-02 | 6.13E-08 | 2.63E-08 | 7.72E-08 | | 3.01E-02 | 2.63E-03 |
| LCPC-$ImClO_4P$ | 1.66E-01 | 3.86E-01 | 7.45E-01 | 5.46E-04 | 2.93E-04 | 6.45E-04 | 3.01E-02 | | 3.82E-01 |
| LCPC-$ImClO_4N$ | 2.45E-02 | 8.25E-02 | 2.31E-01 | 8.88E-03 | 5.37E-03 | 1.02E-02 | 2.63E-03 | 3.82E-01 | |

**Table 3. Multiple comparison of means test results for the speeds of sound in air; p-values <0.05 are shaded in dark red and indicate the average values are different at the 95% confidence level, while p-values shaded in green show no statistical difference.**

| | $ImClO_4$ | $ImClO_4P$ | $ImClO_4N$ | PBA-$ImClO_4$ | PBA-$ImClO_4P$ | PBA-$ImClO_4N$ | LCPC-$ImClO_4$ | LCPC-$ImClO_4P$ | LCPC-$ImClO_4N$ |
|---|---|---|---|---|---|---|---|---|---|
| $ImClO_4$ | | 1.40E-01 | 3.00E-01 | 4.49E-02 | 5.20E-01 | 9.65E-01 | 6.85E-01 | 2.73E-01 | 1.45E-01 |
| $ImClO_4P$ | 1.40E-01 | | 6.59E-01 | 5.88E-04 | 4.03E-01 | 1.52E-01 | 6.33E-02 | 7.03E-01 | 9.86E-01 |
| $ImClO_4N$ | 3.00E-01 | 6.59E-01 | | 2.57E-03 | 6.93E-01 | 3.21E-01 | 1.54E-01 | 9.52E-01 | 6.71E-01 |
| PBA-$ImClO_4$ | 4.49E-02 | 5.88E-04 | 2.57E-03 | | 8.45E-03 | 4.05E-02 | 1.14E-01 | 2.12E-03 | 6.25E-04 |
| PBA-$ImClO_4P$ | 5.20E-01 | 4.03E-01 | 6.93E-01 | 8.45E-03 | | 5.49E-01 | 2.99E-01 | 6.49E-01 | 4.13E-01 |
| PBA-$ImClO_4N$ | 9.65E-01 | 1.52E-01 | 3.21E-01 | 4.05E-02 | 5.49E-01 | | 6.54E-01 | 2.92E-01 | 1.57E-01 |
| LCPC-$ImClO_4$ | 6.85E-01 | 6.33E-02 | 1.54E-01 | 1.14E-01 | 2.99E-01 | 6.54E-01 | | 1.37E-01 | 6.57E-02 |
| LCPC-$ImClO_4P$ | 2.73E-01 | 7.03E-01 | 9.52E-01 | 2.12E-03 | 6.49E-01 | 2.92E-01 | 1.37E-01 | | 7.16E-01 |
| LCPC-$ImClO_4N$ | 1.45E-01 | 9.86E-01 | 6.71E-01 | 6.25E-04 | 4.13E-01 | 1.57E-01 | 6.57E-02 | 7.16E-01 | |

## 3.2 Estimated Detonation Velocities

The predicted detonation velocity for $ImClO_4$ based on a machine learning model for energetic ferroelectric materials (described in Hu et al.[7] with partial results presented in the supplementary material) is 7.29 km/s.[18] Using the calculated density[19] of 1.719 g/cm$^3$ and the predicted heat of formation[18] of 76.13 kJ/mol, the predicted detonation velocity from CHEETAH[20] for $ImClO_4$ at TMD is 7.53 km/s. The estimated detonation velocities from LASEM were determined using the empirically observed correlation between the characteristic laser-induced shock velocities and measured detonation velocities for conventional military explosives[21] and are shown in Figure 6 along with the predicted detonation velocities for $ImClO_4$. The estimated detonation velocities for $ImClO_4$ and PBA-$ImClO_4$ decrease in the presence of the external magnetic field, while they increase slightly for LCPC-$ImClO_4$.

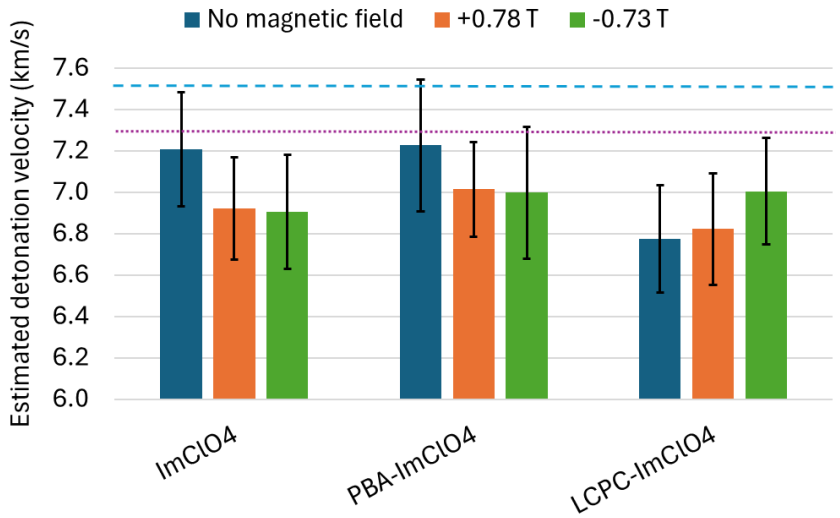


**Figure 6. Comparison of the estimated detonation velocities for the $ImClO_4$, PBA-$ImClO_4$, and LCPC-$ImClO_4$ with (orange = +0.78 T, green = –0.73 T) and without (blue) an external magnetic field. The light-blue dashed line is the predicted detonation velocity for $ImClO_4$ from CHEETAH[20] and the purple dotted line is the predicted detonation velocity for $ImClO_4$ from a machine learning model for energetic ferroelectric materials.[7,18]**

## 3.3 Laser-Induced Plasma Emission

The time-integrated laser-induced plasma emission spectra for each sample with and without the magnetic field are shown in Figure 7. In addition to the expected emission features from carbon (C), cyano radical (CN), hydrogen (H), nitrogen (N), oxygen (O), and chlorine (Cl), emission features from impurities such as sodium (Na) and calcium (Ca) were observed in the $ImClO_4$ spectra (Figure 7a). In contrast with previous studies with this material,[1] emission lines from aluminum (Al) were

also observed, suggesting the selected $ImClO_4$ crystal had some minor metal contamination (a few ppm or less). Many of the emission intensities for $ImClO_4$, PBA-$ImClO_4$, and LCPC-$ImClO_4$ increased in the presence of the magnetic field. LCPC contains lithium (Li) and chromium (Cr), while PBA contains vanadium (V) and Cr (as well as some Li impurity). Figure 8 shows the background-corrected emission intensities for many species after normalization to the total emission intensity. While the C, H, N (not shown), and O intensities increased for all samples under the magnetic field, the Cl intensities remained constant for $ImClO_4$ and PBA-$ImClO_4$ and decreased for LCPC-$ImClO_4$. The Cr and V intensities decreased for the magnet-in-ferroelectric composites with the magnetic fields, while Li increased for PBA-$ImClO_4$ and decreased for LCPC-$ImClO_4$. The molecular emission from CN formed via recombination reactions decreased for $ImClO_4$ in the magnetic field and increased for LCPC-$ImClO_4$—the strong V emission in PBA-$ImClO_4$ obscured the CN bands.

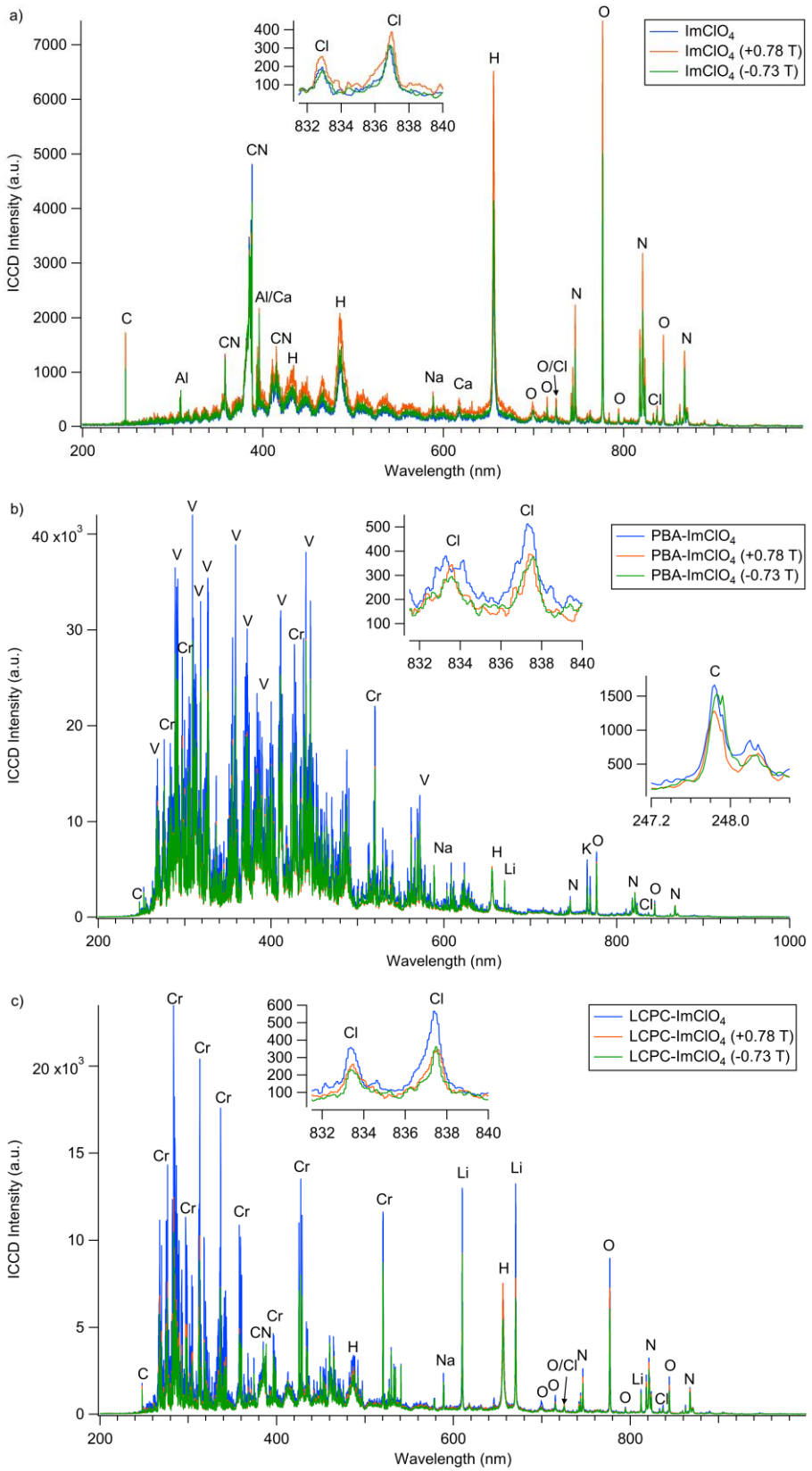


**Figure 7. Laser-induced plasma spectra for the a) $ImClO_4$, b) PBA-$ImClO_4$, and c) LCPC-$ImClO_4$ with and without an external magnetic field.**

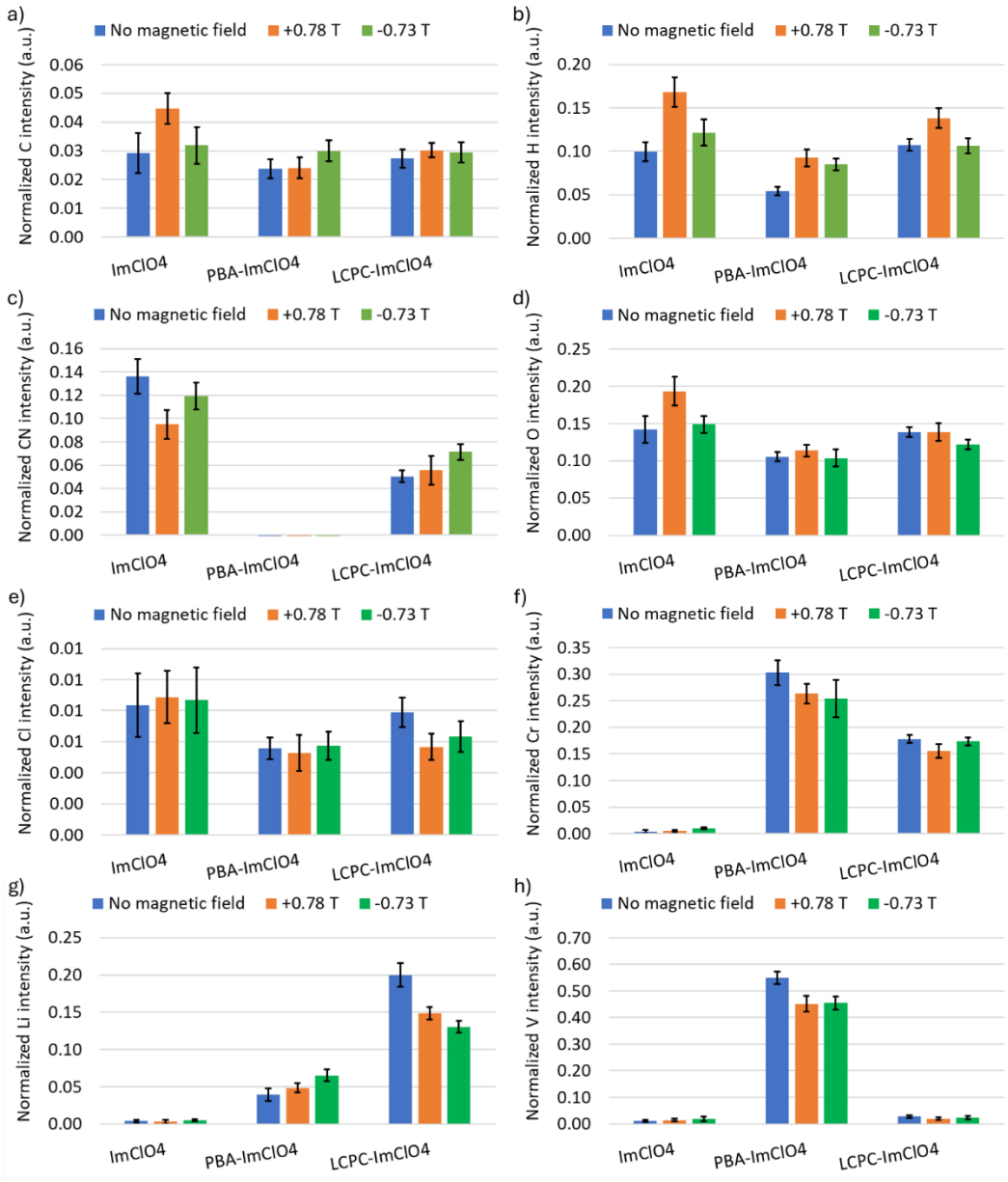


**Figure 8. Normalized, background-corrected emission intensities for a) C (247.86 nm), b) H (656.29 nm), c) CN (388.34 nm), d) O (777.19/42 nm), e) Cl (837.59 nm), f) Cr (520.84 nm), g) Li (670.78 nm), and h) V (309.31 nm) from the laser-induced plasma spectra of $ImClO_4$, PBA-$ImClO_4$, and LCPC-$ImClO_4$ with (either +0.78 T [orange] or –0.73 T [green]) or without (blue) an external magnetic field.**

Plasma excitation temperatures calculated based on the relative intensities of the H lines (434.05, 486.14, and 656.28 nm) are shown in Figure 9. We have shown that for conventional military explosives, these plasma excitation temperatures directly correlate to predicted detonation temperatures.[6] The predicted detonation temperature at TMD from CHEETAH[20] for $ImClO_4$ is 3547.4 K. The estimated detonation temperature based on the plasma excitation temperature is 3770.0 K.

Both the plasma excitation temperatures and estimated detonation temperatures slightly decrease in the presence of the external magnetic field for all samples. The estimated detonation temperatures for the magnet-in-ferroelectric composites are significantly higher than that of neat $ImClO_4$. Energetic formulations with Al as an additive also show increased plasma excitation (i.e., estimated detonation) temperatures.[22–25] The plasma electron density calculated based on the full width at half area of the averaged 656.28 nm $H_\alpha$ line using the method of Gigosos et al.[26] is shown in Figure 10. The presence of the magnetic field decreases the electron density, especially for PBA-$ImClO_4$.

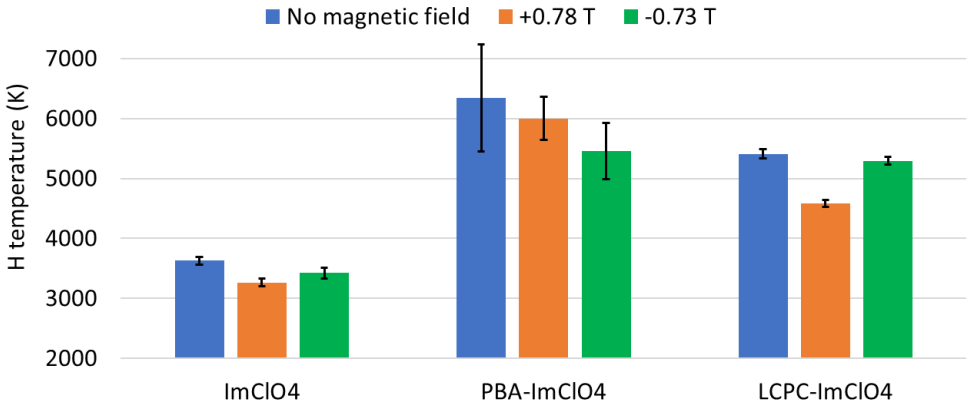


**Figure 9. Comparison of excitation plasma temperatures calculated based on the relative intensities of the H emission intensities from the laser-induced plasma spectra of the $ImClO_4$, PBA-$ImClO_4$, and LCPC-$ImClO_4$ with (either +0.78 T [orange] or –0.73 T [green]) or without (blue) an external magnetic field.**

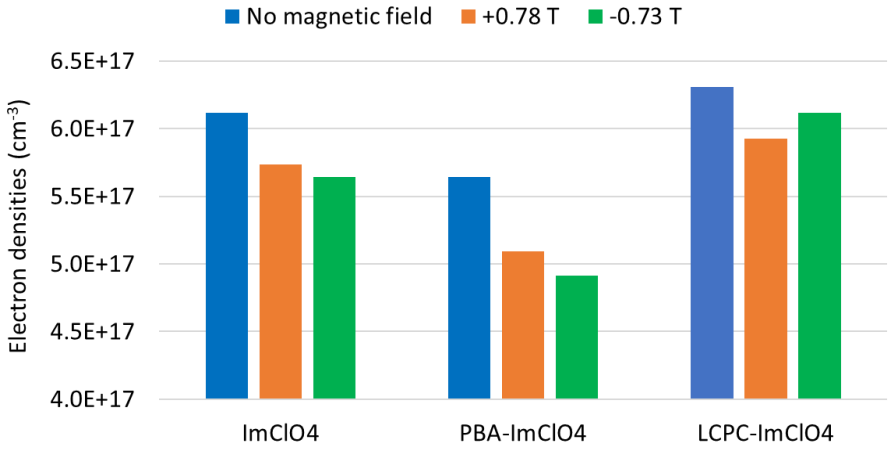


**Figure 10. Comparison of electron densities calculated based on the $H_\alpha$ line widths from the laser-induced plasma spectra of the $ImClO_4$, PBA-$ImClO_4$, and LCPC-$ImClO_4$ with (either +0.78 T [orange] or –0.73 T [green]) or without (blue) an external magnetic field.**

## 3.4 Post-Plasma Combustion Emission

Following cessation of the laser-induced plasma (as indicated by the disappearance of ionized species and emission from high-energy excited states), particles ejected from the sample surface continue to be ignited by the high-temperature region above the sample surface. This time regime (tens to hundreds of microseconds) thus consists of high-temperature combustion reactions. The post-plasma combustion spectra are shown in Figure 11. Under the influence of the –0.73 T field, additional metal impurity lines appeared, including some weak Cr lines (inset of Figure 11a) and some unidentified lines near 317, 327, and 623 nm. The alkali emission features, including Li and potassium (K) become more prominent due to the continual re-excitation of the atoms during the combustion reactions. Molecular features such as the CN bands also become stronger as more recombination reactions occur under the cooler post-plasma combustion conditions (compared with the laser-induced plasma). Additional emission lines also appear in the LCPC-$ImClO_4$ post-plasma combustion spectrum near 309 nm in the –0.73 T magnetic field—the position of these lines appear to be shifted approximately –0.04 nm from the normal Al lines positions (Figure 11c).

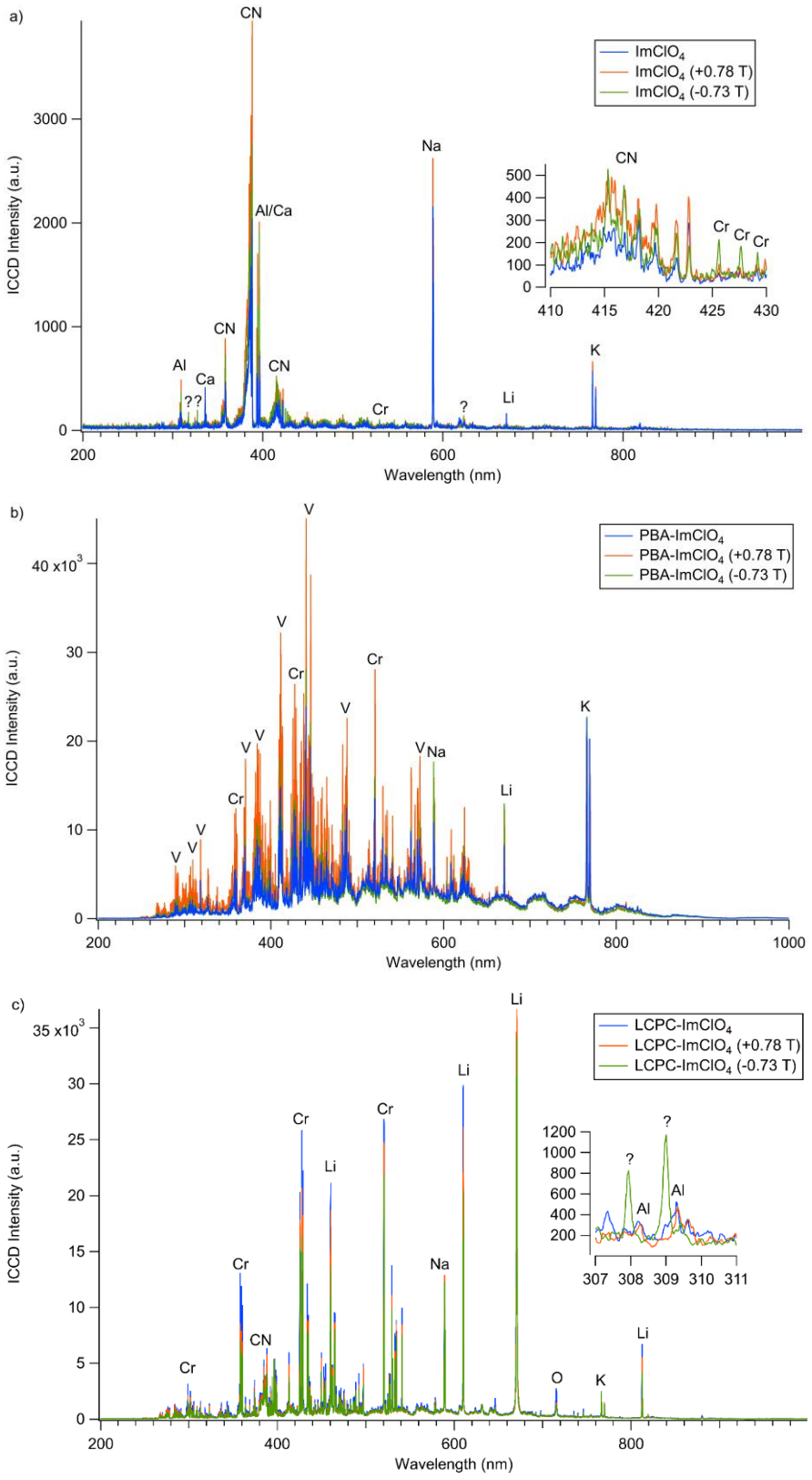


**Figure 11. Post-plasma combustion spectra for the a) $ImClO_4$, b) PBA-$ImClO_4$, and c) LCPC-$ImClO_4$ with and without an external magnetic field.**

The background-corrected emission intensities normalized to the total emission from the post-plasma combustion spectra are shown in Figure 12. In this time regime, the CN intensities stay the same or slightly increase for $ImClO_4$ under the magnetic field, while they slightly decrease for LCPC-$ImClO_4$ (Figure 12a), opposite the trend observed in the laser-induced plasma (Figure 8c). The H and O intensities decrease under the magnetic field for $ImClO_4$ and PBA-$ImClO_4$ and stay nearly the same for LCPC-$ImClO_4$ (Figures 12b and 12c). Generally, the Li intensities increase and the Cr intensities stay about the same under the magnetic field (Figure 12d,e). The V intensities for PBA-$ImClO_4$ increase significantly under +0.78 T but decrease slightly under –0.73 T (Figure 12f). The Al lines in $ImClO_4$ occur at the same location as the selected V line, as does the shifted Al line in the LCPC-$ImClO_4$ spectrum.

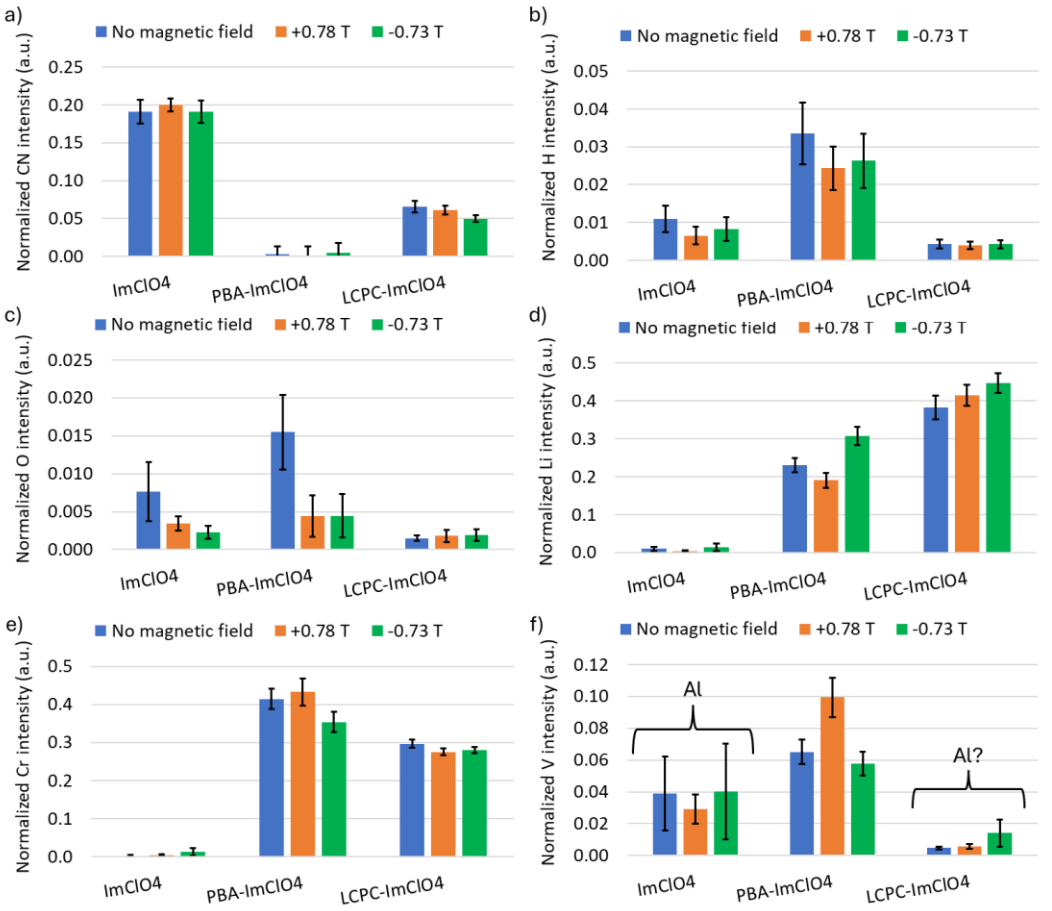


**Figure 12. Normalized, background-corrected emission intensities for a) CN (388.34 nm), b) H (656.29 nm), c) O (777.19/42 nm), d) Li (670.78 nm), e) Cr (520.84 nm), and f) V (309.31 nm) from the post-plasma combustion spectra of $ImClO_4$, PBA-$ImClO_4$, and LCPC-$ImClO_4$ with (either +0.78 T [orange] or –0.73 T [green]) or without (blue) an external magnetic field.**

Although the H emission lines are too weak to calculate the plasma excitation temperatures in the post-plasma combustion regime, the vibrational temperatures

were calculated based on the relative intensities of the CN (384.91, 385.32, 386.03, 387.00, and 388.22 nm) lines, as shown in Figure 13. Because of the long integration time and lack of local thermodynamic equilibrium, the absolute values of these temperatures are not accurate and only provide a rough comparison of temperatures with and without the magnetic field. As observed with the plasma excitation temperatures (Figure 9), the presence of the magnetic field slightly decreases the vibrational temperatures in the post-plasma combustion regime.

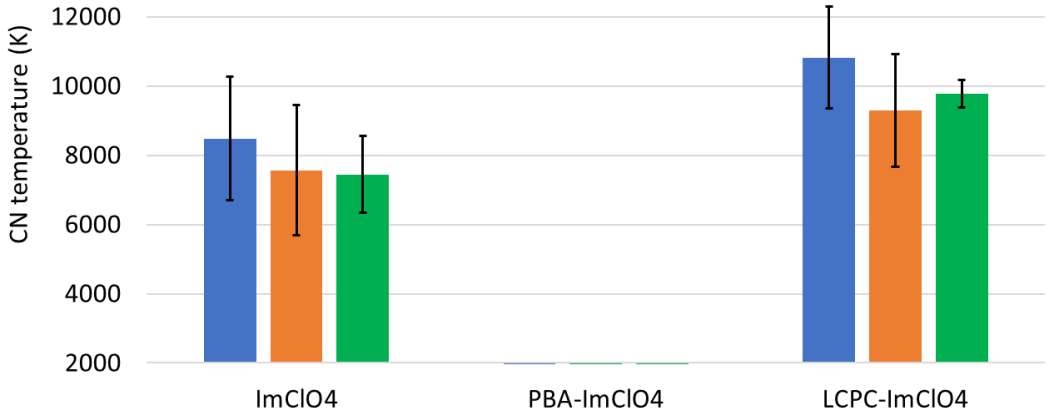


**Figure 13. Comparison of vibrational temperatures calculated based on the relative intensities of the CN emission intensities from the post-plasma combustion of the $ImClO_4$, PBA-$ImClO_4$, and LCPC-$ImClO_4$ with (either +0.78 T [orange] or –0.73 T [green]) or without (blue) an external magnetic field.**

## 3.5 Self-Sustained Combustion Emission

The spectra from the self-sustained combustion reactions on the millisecond timescale are shown in Figure 14. Spectra in this region are typically dominated by broadband blackbody radiation from the burning particles as well as having strong molecular emission bands like the hydroxyl radical (OH). As in the post-plasma combustion spectra, emission lines from alkali species are particularly strong due to continual re-excitation during the combustion reactions. The y-axes for the different samples were kept constant for the three samples for comparison of the combustion emission intensities. None of the samples have significant combustion intensities in this regime (500 µs to 10.5 ms), but the LCPC-$ImClO_4$ without the magnetic field has the strongest self-sustained combustion. In contrast to the LCPC-$ImClO_4$ (Figure 14c), adding the external magnetic field increased the combustion for $ImClO_4$ (Figure 14a) and PBA-$ImClO_4$ (Figure 14b).

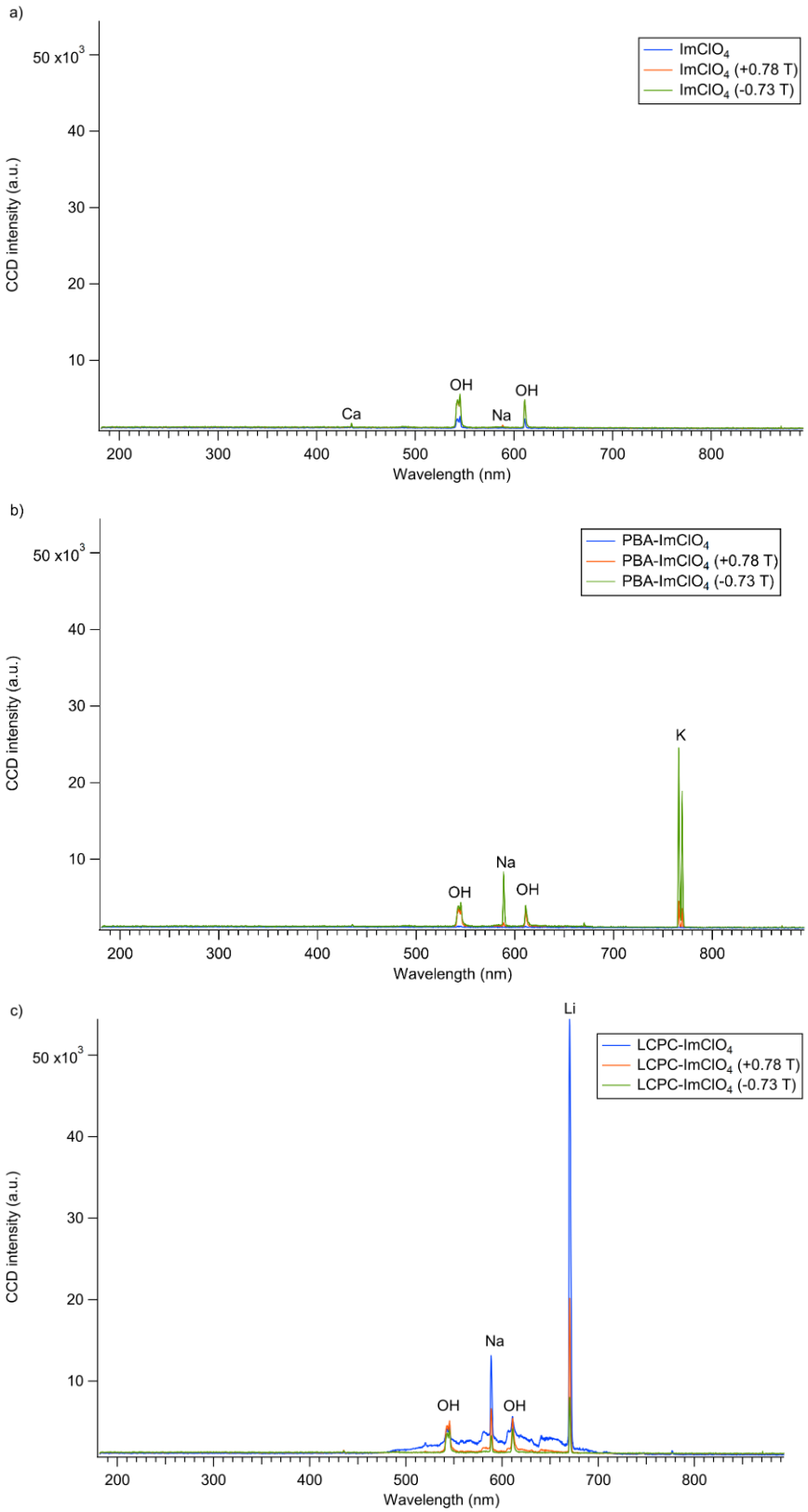


**Figure 14. Self-sustained combustion spectra for the a) $ImClO_4$, b) PBA-$ImClO_4$, and c) LCPC-$ImClO_4$ with and without an external magnetic field.**

The time-resolved combustion emission integrated over the IR region (900–1700 nm) is shown in Figure 15. The graphs on the left are zoomed in to the microsecond timescale to show early combustion reactions, while the graphs on the right show the entire 10-ms duration recorded. Unlike the magnet-in-ferroelectric composites, the $ImClO_4$ has no significant post-plasma emission—although the combustion at the tail end of the plasma emission was enhanced by the magnetic field. The post-plasma combustion emission for PBA-$ImClO_4$ and LCPC-$ImClO_4$ was decreased by the magnetic field. In contrast to the increased visible emission observed in the PBA-$ImClO_4$ in the presence of the magnetic field, the –0.73 T field increases the IR combustion emission.

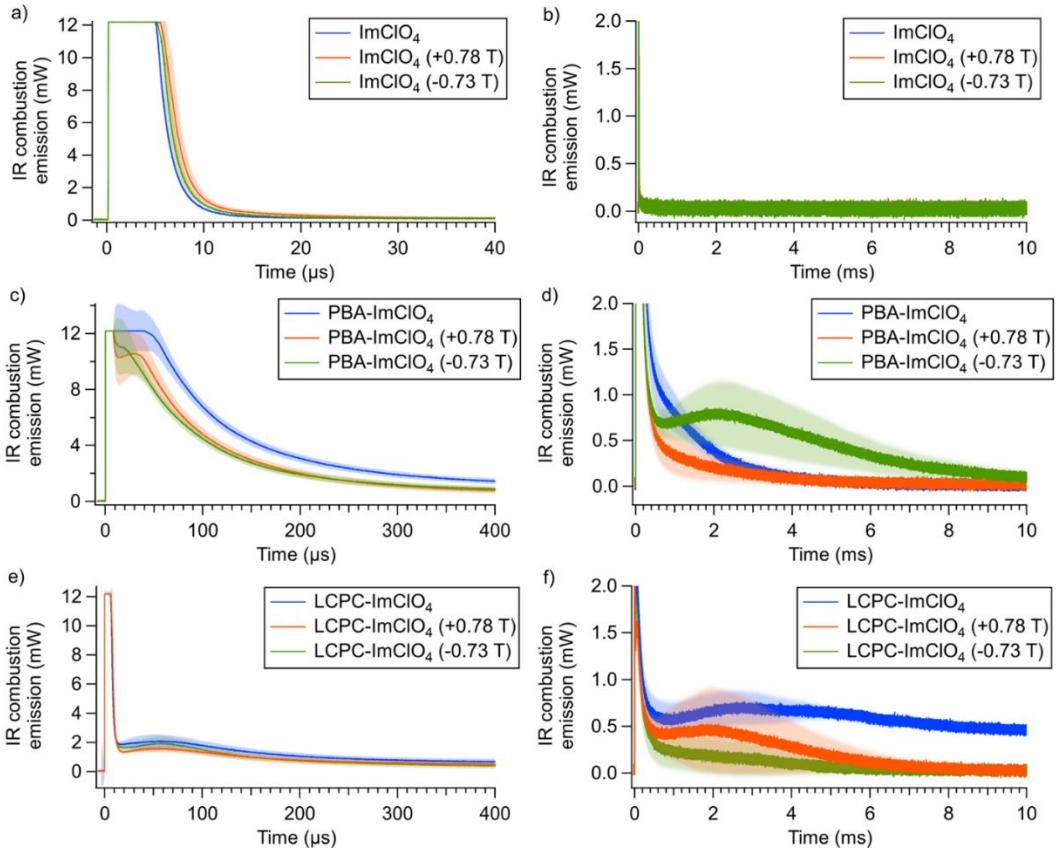


**Figure 15. Time-resolved IR combustion emission from the post-plasma (left) and self-sustained (right) combustion for the $ImClO_4$ (a,b), PBA-$ImClO_4$ (c,d), and LCPC-$ImClO_4$ (e,f) with and without an external magnetic field.**

## 4. Conclusions

The energy release from neat $ImClO_4$ and two different $ImClO_4$-based magnet-in-ferroelectric composites was compared with and without the presence of a strong magnetic field using B-LASEM. While little laser-induced plasma emission was observed for neat $ImClO_4$, both VBA-$ImClO_4$ and LCPC-$ImClO_4$ had stronger,

longer-lasting emission. The Dewey shock velocities for neat PBA-$ImClO_4$ and both magnet-in-ferroelectric composites in the presence of the magnetic field were higher than that of neat $ImClO_4$, indicative of greater energy release later in the plasma lifetime. The estimated detonation velocity (7.21 ±0.25 km/s) and estimated detonation temperature (3770.0 K) for $ImClO_4$ agrees reasonably well to the values predicted by CHEETAH (7.53 km/s and 3547.4 K), although the predicted velocity is slightly higher than the estimated value. The estimated detonation velocity (7.23 ±0.23 km/s) for VBA-$ImClO_4$ is similar to that for $ImClO_4$, although the estimated detonation temperature is significantly higher (9633.6 K). The estimated detonation velocity (6.78 ±0.18 km/s) for LCPC-$ImClO_4$ is lower than that for $ImClO_4$, while the estimated detonation temperature is significantly higher (7617.2 K). The neat $ImClO_4$ had very little post-plasma or self-sustained combustion emission, but the composites had significant combustion reactions.

When comparing the energy release of the samples without and with the magnetic field present, it was observed that the magnetic field increased the speed of sound in air (i.e., the air surrounding the reaction region was heated more). However, the estimated detonation temperatures (microsecond timescale) were lower for all samples in the presence of the magnetic field. The laser-induced plasma emission intensities for the organic species generally increased for all samples in the magnetic field, while those for the metallic species generally decreased. The plasma electron densities decreased in the presence of the magnetic field, in sharp contrast to those for neat metallic samples such as Al, iron (Fe), and copper (Cu)[12]—where significant increases in electron density were observed in the presence of the magnetic field.

Evidence for stronger magnetic coupling with LCPC-$ImClO_4$ compared with the other samples included the observations that adding an external magnetic field lowers the characteristic laser-induced shock velocity for the neat $ImClO_4$ and for the PBA-$ImClO_4$—but does not significantly affect the Dewey shock velocity. In contrast, the characteristic laser-induced shock velocities increase for LCPC-$ImClO_4$ in the presence of the magnetic field—as do the Dewey shock velocities. Consequently, the estimated detonation velocities were lower for all samples in the presence of the magnetic field, except for LCPC-$ImClO_4$. Finally, while the CN emission intensities from the laser-induced plasma decreased for the $ImClO_4$ and VBA-$ImClO_4$, they increased for LCPC-$ImClO_4$. Models that include the chemical reaction kinetics under the influence of magnetic coupling may provide further insight into the changes in reaction mechanisms that resulted in the observed differences in LCPC-$ImClO_4$ behavior following rapid heating under the influence of the magnetic field. Our results demonstrate magnetic coupling can be used to

influence when and how much energy is released by energetic materials under detonation-like conditions.

## 5. References


1. Gottfried JL, Wu C-C, Pesce-Rodriguez RA, Walck SD, Ren S. Imidazolium perchlorate: a novel energetic molecular ferroelectric. DEVCOM Army Research Laboratory (US); 2021. Report No.: ARL-TR-9289.
2. Hu Y et al. Chemically driven energetic molecular ferroelectrics. Nature Comm. 2021;12:5696.
3. Huang Y et al. Proton-controlled molecular ionic ferroelectrics. Nature Comm. 2023;14(1):5041.
4. Gottfried JL, Pesce-Rodriguez RA, Wu C-C, Walck SD, Ren S. Characterization of energetic molecular ferroelectric materials. JANNAF; 2023 May 22–26; Pittsburgh, PA. (Presentation/paper is CUI)
5. Gao W et al. Flexible organic ferroelectric films with a large piezoelectric response. NPG Asia Mater. 2015;7(6):e189–e189.
6. Gottfried JL, Wainwright ER. Laser-induced air shock from energetic materials (LASEM): a novel microscale technique for characterizing energy release at high heating rates. J Energ Mater. 2023;43(1):1–61.
7. Hu Y et al. Releasing chemical energy in spatially programmed ferroelectrics. Nature Comm. 2022;13(1):6959.
8. Wang ZX et al. Magnet-in-ferroelectric crystals exhibiting photomultiferroicity. PNAS. 2024;121(17):7.
9. Huang Y et al. Pressure-controlled magnetism in 2D molecular layers. Nature Comm. 2023;14(1):3186.
10. Jalouli A, Ren S. Magnetoelectric interaction in molecular multiferroic nanocomposites. RSC Adv. 2022;12(37):24050–24054.
11. Gottfried JL, Dillier CA, Wainwright ER. External magnetic field effects on the energy release from laser-ablated ferromagnetic, paramagnetic, and diamagnetic metals, Part I: plates vs. powders under extremely weak magnetic fields. DEVCOM Army Research Laboratory (US); 2024 Aug. Report No.: ARL-TR-9958. (Report is CUI)

12. Gottfried JL, Dillier CAM. External magnetic field effects on the energy release from laser-ablated ferromagnetic, paramagnetic, and diamagnetic metals, Part II: powders under moderately strong magnetic fields. DEVCOM Army Research Laboratory (US); 2025 June. Report No.: ARL-TR-10110. (Report is CUI)

13. Gottfried JL, Dillier CAM, Wainwright ER. Automated shock wave measurement and fitting for the LASEM-420 system, Part I: description of Matlab codes. DEVCOM Army Research Laboratory (US); 2023 Aug. Report No.: ARL-TR-9738. (Report is CUI)

14. Gottfried JL, Dillier CAM, Wainwright ER. Automated shock wave measurement and fitting for the LASEM-420 system, Part II: comparison of explosive data. DEVCOM Army Research Laboratory (US); 2023 Aug. Report No.: ARL-TR-9756. (Report is CUI)

15. Gottfried JL. Automated shock wave measurement and fitting for the LASEM-420 system, Part III: influence of pixel rounding errors. DEVCOM Army Research Laboratory (US); 2023 Dec. Report No.: ARL-TN-1184. (Report is CUI)

16. Gottfried JL, Barnes BC. Higher time-resolution LASEM, Part II: influence of plasma chemistry on the laser-induced shock waves of explosives. DEVCOM Army Research Laboratory (US); 2020 Aug. Report No.: ARL-TR-9026.

17. Gottfried JL. Automated shock wave measurement and fitting for the LASEM-420 system, Part IV: statistical significance of calculated parameters. DEVCOM Army Research Laboratory (US); 2024 Nov. Report No.: ARL-TN-1233. (Report is CUI)

18. Ren S. SUNY University at Buffalo. Personal communication, 2023 Feb 12.

19. Pająk Z, Czarnecki P, Szafrańska B, Małuszyńska H, Fojud Z. Ferroelectric ordering in imidazolium perchlorate. J Chem Phys. 2006;124(14):144502.

20. Bastea S et al. CHEETAH 10.1. Energetic Materials Center, Lawrence Livermore National Laboratory; 2022. (Software is CUI)

21. Gottfried JL. Estimated detonation performance of military explosives using higher time-resolution laser-induced air shock from energetic materials (LASEM-420): investigation of particle size effects for RDX and HMX. DEVCOM Army Research Laboratory (US); 2025 Mar. Report No.: ARL-TR-10073. (Report is CUI)

22. Gottfried JL. Higher time-resolution LASEM, part III: influence of laser-induced plasma chemistry on the laser-induced shock waves of aluminized explosives. DEVCOM Army Research Laboratory (US); 2020 Aug. Report No.: ARL-TR-9025.

23. Gottfried JL, Dillier CA, Pesce-Rodriguez R, Wainwright ER, Giri L. Influence of formulation ingredients on aluminum reactivity, Part I: particle size effects for ammonium perchlorate stimulated at high heating rates. DEVCOM Army Research Laboratory (US); 2024 May. Report No.: ARL-TR-9910. (Report is CUI)

24. Gottfried JL, Dillier CA, Wainwright ER. Influence of formulation ingredients on aluminum reactivity, Part II: oxidizer and binder effects at high heating rates. DEVCOM Army Research Laboratory (US); 2024 Aug. Report No.: ARL-TR-9950. (Report is CUI)

25. Gottfried JL, Dillier CA, Wainwright ER. Influence of formulation ingredients on aluminum reactivity, Part III: explosive effects at high heating rates. DEVCOM Army Research Laboratory (US); 2024 Sep. Report No.: ARL-TR-9976. (Report is CUI)

26. Gigosos MA, González MÁ, Cardeñoso Vn. Computer simulated Balmer-alpha, -beta and -gamma Stark line profiles for non-equilibrium plasmas diagnostics. Spectrochim Acta B. 2003;58(8):1489–1504.

## List of Symbols, Abbreviations, and Acronyms

| | |
|---|---|
| 2-D | two-dimensional |
| Al | aluminum |
| C | carbon |
| Ca | calcium |
| CCD | charge-coupled device |
| Cl | chlorine |
| CN | cyano radical |
| Cr | chromium |
| DDG | digital delay generator |
| H | hydrogen |
| $H_2O$ | water |
| HNS | hexanitrostilbene |
| ICCD | intensified charge-coupled device |
| $ImClO_4$ | imidazolium perchlorate |
| IR | infrared |
| K | potassium |
| LASEM | laser-induced air shock from energetic materials |
| Li | lithium |
| N | nitrogen |
| Na | sodium |
| O | oxygen |
| OH | hydroxyl radical |
| RGB | red–green–blue |
| TMD | theoretical maximum density |
| V | vanadium |

| | |
|---|---|
| 1 (PDF) | DEFENSE TECHNICAL INFORMATION CTR DTIC OCA |
| 1 (PDF) | DEVCOM ARL FCDD RLB CI TECH LIB |